Check for updates

View Article Online
View Journal

Dalton Transactions

Accepted Manuscript

This article can be cited before page numbers have been issued, to do this please use: D. Markad, S. Khullar and S. Mandal, *Dalton Trans.*, 2019, DOI: 10.1039/C8DT04773A.

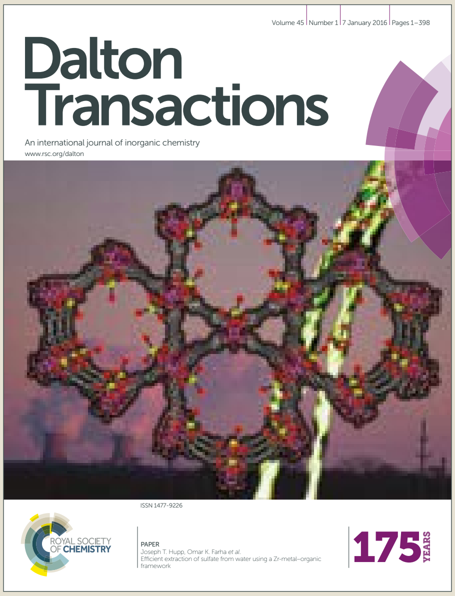

Volume 45 | Number 1 | 7 January 2016 | Pages 1–398

Dalton Transactions

An international journal of inorganic chemistry
www.rsc.org/dalton

ISSN 1477-9226

ROYAL SOCIETY OF CHEMISTRY

PAPER
Joseph T. Hupp, Omar K. Farha et al.
Efficient extraction of sulfate from water using a Zr-metal–organic framework

175 YEARS

This is an Accepted Manuscript, which has been through the Royal Society of Chemistry peer review process and has been accepted for publication.

Accepted Manuscripts are published online shortly after acceptance, before technical editing, formatting and proof reading. Using this free service, authors can make their results available to the community, in citable form, before we publish the edited article. We will replace this Accepted Manuscript with the edited and formatted Advance Article as soon as it is available.

You can find more information about Accepted Manuscripts in the author guidelines.

Please note that technical editing may introduce minor changes to the text and/or graphics, which may alter content. The journal's standard Terms & Conditions and the ethical guidelines, outlined in our author and reviewer resource centre, still apply. In no event shall the Royal Society of Chemistry be held responsible for any errors or omissions in this Accepted Manuscript or any consequences arising from the use of any information it contains.

ROYAL SOCIETY OF CHEMISTRY

rsc.li/dalton

View Article Online
DOI: 10.1039/C8DT04773A

Journal Name

ARTICLE

Received 00th January 20xx,
Accepted 00th January 20xx

DOI: 10.1039/x0xx00000x

www.rsc.org/

Novel primary amide-based cationic metal complexes: green synthesis, crystal structures, Hirshfeld surface analysis and solvent-free cyanosilylation reaction†

Datta Markad,[a] Sadhika Khullar [b] and Sanjay K. Mandal *[a]

A new symmetrical and flexible primary amide functionalized ligand, 2,2'-(ethane-1,2-diylbis((pyridin-2-ylmethyl)azanediyl))diacetamide (**2-BPEG**), has been synthesized and structurally characterized. Using this multidenate ligand, four novel metal complexes, namely $[Cu(2\text{-}BPEG)](ClO_4)_2{\cdot}0.5H_2O$ (**1**), $[Zn(2\text{-}BPEG)](ClO_4)_2$ (**2**), $[Zn(2\text{-}BPEG)](ZnCl_4){\cdot}H_2O$ (**3**) and $[Cd(2\text{-}BPEG)(H_2O)](ClO_4)_2{\cdot}H_2O$ (**4**), have been synthesized under ambient conditions and characterized by elemental, spectroscopic and thermal analysis, and single and powder X-ray diffraction. Complexes **1**-**3** are hexacoordinated with an N4O2 donor set (provided by the hexadentate 2-BPEG ligand) while Complex **4** is heptacoordinated with an additional coordinated water molecule. In all cases, the 2-BPEG ligand acts as a hexadentae ligand. A change in the starting metal salt has resulted in the formation of **2** and **3** with different tetrahedral anions, ClO_4^- and $ZnCl_4^-$, respectively. This has provided an opportunity to showcase anion-directed supramolcular networks for these compounds. Compounds **1**, **2** and **4** with perchlorate anions show similar and comparable intermolecular interactions in their 3D networks. On the other hand, the supramolecular self-assembly of **3** is dominated by a variety of intermolecular interactions such as C–H···Cl, N–H···Cl, O–H···Cl and C–H···O due to the presence of tetrachlorozincate(II) ion. Moreover, the role of weak intermolecular interactions in the crystal packing has been analysed and quantified using Hirshfeld surface analysis. Furthermore, compound **4** exhibiting open Lewis acid site has been found to be a very efficient and recyclable heterogeneous catalyst for the solvent-free cyanosilylation of various aldehydes with trimethylsilyl cyanide (TMSCN) producing the corresponding trimethylsilyl ether in high yields.

Introduction

Supramolecular chemistry continues to attract great research interest not only for their appealing structures but also due to their diversified applications in various fields such as catalysis, luminescence, gas/vapour sorption and storage, optics, biomedical, electronic and magnetic devices, etc.[1–4] In case of supramolecular coordination architectures, both coordination bonds and non-covalent interactions have been found to be the driving forces.[5–8] Non-covalent interactions, such as hydrogen bonding, electrostatic, π-π stacking, anion-π, etc., are the most prominent binding forces that have been crucial for the formation of such architectures and their crystal packing.[6,7,9–12] Many different self-complementary hydrogen bonding groups like –COOH, –C(O)NH–, $–C(O)NH_2$, –OH, etc., can be used to control association in the solid state and to produce networks with predictable structural features and properties.[13] In this regard, molecular self-assembly - a spontaneous process for setting the disarranged molecules into an organized structure or pattern – has played a key role.[11,12,14,15] Several contributing factors to the designing of supramolecular coordination architectures include metal ions, coordination numbers, ligand geometry, intermolecular interactions, solvent molecules and counter ions as well as the synthesis conditions. A proper understanding of these factors is important not only for rationalizing the solid-state architectures of these compounds but also for enabling the design and prediction of new supramolecular entities.

Among various organic ligands, the use of N/O mixed ligands in the synthesis of coordination compounds has been a trend for a long time.[16–19] However, the anionic ligands are much more explored in the literature compared to the neutral ones.[17,20–26] The coordination of metal ions by amide groups of simple amides, peptides and proteins is of great interest due to the importance of such complexes in biological systems.[27] Besides their obvious biological significance, it provides various possibilities of hydrogen bonding motifs which can be used to control the self-assembly processes between metal complexes

---

[a] *Department of Chemical Sciences, Indian Institute of Science Education and Research Mohali, Sector 81, Manauli PO, S.A.S. Nagar, Mohali, Punjab 140306, INDIA. E-mail: sanjaymandal@iisermohali.ac.in*

[b] *Department of Chemistry, Dr. B R Ambedkar National Institute of Technology, Jalandhar, Punjab 144011, INDIA*

*†Electronic supplementary information (ESI) available: Crystallographic data of **2-BPEG** and **1-4** in CIF format (CCDC 1873833-37, respectively), additional figures (FTIR, NMR, HRMS and SCXRD) for **2-BPEG** and **1-4**. For ESI and crystallographic data in CIF or other electronic format see DOI: 10.1039/x0xx00000x*

View Article Online
DOI: 10.1039/C8DT04773A

in supramolecular coordination chemistry.[14,28] As reported earlier, the flexible primary amide ligands and their derivatives are good candidates for creating supramolecular networks.[29]

In contrast to the large body of information obtained for the secondary amide (-CONH-) functionalized ligand coordination to metal centers, much less is known about the metal complexes of primary amide (-CONH$_2$) ligands, though amino acid residues such as glutamine or asparagine are key components in the structure of proteins.[30–32] Based on a search of the Cambridge Structural Database (CSD version 5.39, November 2018), only 296 primary amide based cationic metal complexes have been structurally characterised; specifically, there are 72, 23 and 9 complexes for copper, zinc and cadmium, respectively.[33] Furthermore, fewer hexacoordinated complexes are found for copper (32), zinc (17) and cadmium (7), where most of the primary amide ligands are bidentate nicotinamides or tetradentate macrocyclic diamides.

In view of the above background, we have designed and synthesized a symmetrical and flexible primary amide functionalized multidentate ligand, 2,2'-(ethane-1,2-diyl bis((pyridin-2-ylmethyl)azanediyl))diacetamide (**2-BPEG**) with the following considerations (Fig. 1): (a) it can coordinate to the metal center through oxygen atoms and the uncoordinated NH$_2$ moieties can furnish good hydrogen bond donor sites, and (b) it can bind to either a single metal center (hexacoordination) or span between two metal centers in a *bis*(tridentate) mode. In addition, the pyridyl moiety in a ligand is a good candidate for generating higher dimensional coordination compounds because in addition to its coordination to a metal ion through the nitrogen atom it can also provide an identification site for π-π stacking interactions to generate 3D supramolecular networks.[34] We have chosen Cu(II), Zn(II) and Cd(II) to make cationic complexes for their rarity.

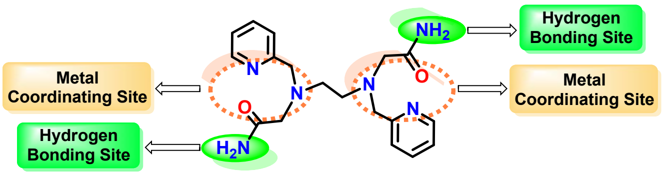

Fig. 1 Structure of 2,2'-(ethane-1,2-diylbis((pyridin-2-ylmethyl)azanediyl)) diacetamide (**2-BPEG**) with its metal coordinating sites and hydrogen bonding sites labelled.

For exploring an understanding of intermolecular interactions in the supramolecular assemblies, it is crucial to have quantitative measurements of these interactions. Hirshfeld surface analysis[35,36] has become a valuable tool for elucidating molecular crystal structures quantitatively. Unfortunately, such quantitative measures of weak interactions in primary amide based metal complexes are poorly documented in the literature.[37]

One of the desired applications of functional supramolecular coordination architectures is their use as heterogeneous catalysts in the C–C and C–N bond forming reactions. For a compound acting as a heterogeneous catalyst in a chemical process, it has to be insoluble in the preferred and low-cost solvents. A strong industrial preference for heterogeneous catalysts arises from their inherent stability and ease of recovery, allowing for more efficient separation and recycling. On the other hand, a pressing challenge for catalysis in organic synthesis complying with the green chemistry concept is to advance new processes that are efficient, high yielding and environmentally friendly. Therefore, the ideal strategy to reduce their impact on the environment is to conduct the reaction with a heterogeneous catalyst under solvent-free conditions. The cyanosilylation of carbonyl compounds with trimethylsilyl cyanide (TMSCN) is a direct and efficient method for the synthesis of trimethylsilyl ethers, precursors of cyanohydrins. The importance of cyanohydrins is due to its easy conversion into biologically important compounds, such as β-amino alcohols, α-hydroxy acids, α-hydroxyl ketones and α-amino acids.[38,39] Various discrete complexes and coordination polymers have been used as homogeneous catalysts for this reaction;[40-44] however, only a limited number of heterogeneous catalysts is reported.[41,45-55] Furthermore, the scope for developing a heterogeneous catalyst for the solvent-free cyanosilylation reaction is wide open. To the best of our knowledge, the use of a Cd(II) mononuclear complex as a heterogeneous catalyst for cyanosilylation of aldehydes under solvent-free conditions has not been reported. Thus, the development of such Cd(II) catalysts for cyanosilylation of carbonyl compounds with TMSCN is highly desired.

Herein, we report the synthesis, structural characterization and physicochemical properties of **2-BPEG** and its metal complexes, namely [Cu(2-BPEG)](ClO$_4$)$_2$·0.5H$_2$O (**1**), [Zn(2-BPEG)](ClO$_4$)$_2$ (**2**), [Zn(2-BPEG)](ZnCl$_4$)·H$_2$O (**3**) and [Cd(2-BPEG)(H$_2$O)](ClO$_4$)$_2$·H$_2$O (**4**), with the help of a number of analytical techniques, such as single crystal X-ray diffraction (SCXRD), Fourier-transform infrared (FTIR) spectroscopy, UV-Visible spectroscopy (UV-Vis), thermogravimetric analysis (TGA), differential thermal analysis (DTA) and powder X-ray diffraction (PXRD). Hirshfeld surface analysis employing 3D molecular surface contours and 2D fingerprint plots have been used to analyze intermolecular interactions present in the solid state structures of **2-BPEG** and compounds **1**-**4**. Furthermore, compound **4** exhibiting an open Lewis acid site has been established as an efficient and recyclable heterogeneous catalyst for the solvent-free cyanosilylation of various aldehydes with trimethylsilyl cyanide (TMSCN), producing the corresponding trimethylsilyl ether in high yields.

Experimental section

Materials and methods

Metal salts and other reagent grade chemicals were procured from Sigma-Aldrich and were used as received. All solvents were obtained from Merck, India. These solvents were used without further purification. All reactions were carried out under aerobic conditions. For the ligand **2-BPEG**, the intermediate *N,N'*-*bis*(pyridin-2-ylmethyl)ethane-1,2-diamine (2-BPED) was synthesized by modifying a previously reported procedure.[56]

View Article Online
DOI: 10.1039/C8DT04773A

***Caution!** In this study, metal perchlorates were used without any problem, but special care should be taken to handle such salts, which are dangerous. Only a small amount of the materials should be prepared at a time.*

Physical measurements

The ^{1}H and ^{13}C NMR spectra of **2-BPEG** were recorded on a Bruker ARX-400 (400 and 100 MHz, respectively) spectrometer in $CDCl_3$ at 25 °C; the chemical shifts are reported relative to the residual solvent signals. Melting points were determined using a Büchi M-565 instrument. TGA and DTA were carried out from 30 to 300 °C (at a heating rate of 10 °C min^{-1}) under a dinitrogen atmosphere using a Shimadzu DTG-60H instrument. Elemental analysis (C, H, N) was carried out using a Mettler CHNS analyzer. High Resolution Mass Spectrometry (HRMS) data were measured by Thermo Scientific LTQ XL LC-MS instrument for the 50-2000 amu range with an ESI ion source. Solid state UV-Vis spectra were recorded using an Agilent Technologies Cary 5000 UV-Vis-NIR spectrophotometer. FTIR spectra (KBr pellet, 400–4000 cm^{-1}) were measured on a Perkin-Elmer Spectrum I spectrometer. Powder X-ray diffraction (PXRD) data were collected using a Rigaku Ultima IV diffractometer equipped with a 3 kW sealed tube Cu *Kα* X-ray source (settings: 40 kV and 40 mA) and a DTex Ultra detector using BB geometry. Each sample was ground into a fine powder using a mortar and a pestle and was placed on a glass sample holder that was placed on the sample stage attachment. Data were collected over a 2-theta range of 5° to 50° with a scanning speed of 1° per minute using a 0.01° step.

Synthesis of 2,2'-(ethane-1,2-diylbis((pyridin-2-ylmethyl)azanediyl))diacetamide (2-BPEG)

It is prepared in two steps where 2-BPED is an intermediate.

Step 1, Synthesis of 2-BPED: In a 50 mL two-neck round-bottom flask (RBF), 2-pyridinecarboxaldehyde (1.99 mL, 20.96 mmol) was dissolved in 10 mL of methanol. To this, ethylenediamine (0.7 mL, 10.48 mmol) was added dropwise at room temperature, and the mixture was stirred under an inert atmosphere for 4 h. An excess of sodium borohydride (1.2 g, 1.5 equiv.) was added slowly to it at 0 °C and the reaction mixture was stirred for another 5 h. Extraction of the product with chloroform followed by drying with anhydrous Na_2SO_4 and removal of the solvent under vacuum resulted in a light yellow oily product. Yield: 2.2 g (87%). ^{1}H NMR (400 MHz, $CDCl_3$, δ ppm): 8.57 (2H, d), 7.67 (2H, m), 7.34 (2H, d), 7.18 (2H, m), 3.93 (4H, s), 2.84 (4H, s). ^{13}C NMR (100 MHz, $CDCl_3$, δ ppm): 159.90, 149.30, 136.46, 122.28, 121.92, 55.20, 49.09. Selected FTIR peaks (KBr cm^{-1}): 3306 (br, N–H stretch), 2928 (m, aromatic C–H stretch), 2855 (m), 1592 (s, pyridine C=C stretch), 1570 (s, pyridine C=N stretch), 1471 (m), 1434 (m), 1300 (m, aliphatic C–H stretch), 1118 (m, aliphatic C–C stretch), 1048 (s), 996 (s), 760 (s), 631 (m).

Step 2: To a solution of 2-BPED (968 mg, 4 mmol; 15 mL dry acetonitrile) placed in a 50 mL RBF under N_2 atmosphere, K_2CO_3 (2.76 g, 20 mmol) was added through a funnel at once and allowed to stir for 30 minutes. A solution of 2-bromoacetamide (1.1 g, 8 mmol) in dry acetonitrile (15 mL) was added dropwise to the above mixture. The mixture was heated under reflux for 8 h, allowed to cool down to room temperature, and filtered using a G-4 crucible to collect the liquid phase (the residue was thoroughly washed with 2 X 10 mL methanol). The combined filtrate was evaporated to dryness followed by the extraction of the product with dry methanol and filtration to remove excess K_2CO_3 and KBr (by-product). Upon evaporation of methanol under vacuum resulted in the formation of an oily substance which was cooled to 0 °C and treated with 15 mL $CHCl_3$. Further filtration and evaporation of the solvent resulted in the desired product as a light-yellow solid. Yield: 1.21 g (85%). ^{1}H NMR (400 MHz, $CDCl_3$, δ ppm): 8.56 (2H, d), 8.18 (2H, d), 7.66 (2H, m), 7.22 (2H, t), 7.18 (2H, s), 5.84 (2H, s), 3.74 (4H, s), 3.16 (4H, s), 2.72 (4H, s). ^{13}C NMR (100 MHz, $CDCl_3$, δ ppm): 174.35, 157.84, 149.59, 136.69, 123.24, 122.58, 60.73, 58.09, 52.81. Selected FTIR peaks (KBr cm^{-1}): 3390 (s), 3192 (m), 1656 (s, amide C=O stretch), 1592 (s, pyridine C=C stretch), 1400 (s, pyridine C=N stretch), 1108 (m), 764 (s), 696 (m). UV–Vis (Solid state): λ_{max}, 264 nm M.P.: 166–168 °C. MS (ESI-TOF): *m/z* calcd for $[(2\text{-BPEG})H]^+$, 357.1988; found, 357.1981. Rectangular-shaped crystals suitable for single crystal X-ray study were obtained by dissolving 5 mg of **2-BPEG** in 4 mL methanol and keeping the solution for slow evaporation at room temperature for 7 days.

Synthesis of $[Cu(2\text{-BPEG})](ClO_4)_2{\cdot}0.5H_2O$ (1)

In a 10 mL RBF, $Cu(ClO_4)_2{\cdot}6H_2O$ (26 mg, 0.07 mmol) was dissolved in 4 mL methanol. To this, a clear methanolic solution of 2-BPEG (25 mg, 0.07 mmol; 3 mL methanol) was added with stirring. A resulting clear bluish reaction mixture was stirred for another 5 h at room temperature. A bluish-green solid was isolated after removal of methanol under vacuum and air-dried. Yield: 40 mg (91%). Anal. Calc for $C_{18}H_{25}Cl_2CuN_6O_{10.5}$ (MW 627.88): C, 34.43; H, 4.01; N, 13.39. Found: C, 33.16; H, 4.02; N, 12.96. Selected FTIR peaks (KBr, cm^{-1}): 3448 (br), 3358 (m), 3138 (m), 1670 (s), 1612 (s), 1450 (s), 1110 (s), 1090 (s), 1026 (m), 772 (m), 626 (s). UV–Vis (solid state): λ_{max}, 262 nm. Blue crystals of **1** suitable for single crystal X-ray diffraction analysis were obtained from the slow evaporation of its methanolic solution after 2 days.

Synthesis of $[Zn(2\text{-BPEG})](ClO_4)_2$ (2)

It was prepared following the procedure described above for **1** except $Zn(ClO_4)_2{\cdot}6H_2O$ (26 mg, 0.07 mmol) was used as the metal salt. A light-yellow solid was obtained. Yield: 41 mg (94%). Anal. Calcd for $C_{18}H_{24}Cl_2N_6O_{10}Zn$ (MW 620.70): C, 34.83; H, 3.90; N, 13.54. Found: C, 34.98; H, 3.71; N, 13.82. Selected FTIR peaks (KBr, cm^{-1}): 3466 (m), 3404 (m), 3354 (m), 3294 (m), 1666 (s), 1450 (s), 1320 (s), 1096 (s), 1026 (m), 774 (s), 624 (s). UV–Vis (solid state): λ_{max}, 264 nm. Light yellow crystals of **2** suitable for single crystal X-ray diffraction analysis were obtained from the slow evaporation of its methanolic solution after 3 days.

Synthesis of $[Zn(2\text{-BPEG})](ZnCl_4){\cdot}H_2O$ (3)

It was prepared following the procedure described above for **1** except $ZnCl_2$ (19 mg, 0.14 mmol) was used instead of

View Article Online
DOI: 10.1039/C8DT04774A

$Cu(ClO_4)_2 \cdot 6H_2O$. A light-yellow solid was obtained. Yield: 40 mg (88%). Anal. Calc for $C_{18}H_{26}Cl_4N_6O_3Zn_2$ (MW 646.99): C, 33.41; H, 4.05; N, 12.99. Found: C, 33.80; H, 3.88; N, 13.07. Selected FTIR peaks (KBr, cm^{-1}): 3512 (w), 3358 (m), 3302 (m), 3182 (w), 2928 (m), 1664 (s), 1604 (s), 1450 (m), 1310 (m), 1098 (m), 786 (m), 624 (s). UV–Vis (solid state): λ_{max}, 264 nm. Light yellow crystals of **3** suitable for single crystal X-ray diffraction analysis were obtained from the slow evaporation of its methanolic solution after 3 days.

Synthesis of [Cd(2-BPEG)(H_2O)](ClO_4)$_2$·H_2O (4)

It was prepared following the procedure described above for **1** except $Cd(ClO_4)_2 \cdot xH_2O$ (21.9 mg, 0.070 mmol) was used as the metal salt. A light-yellow solid was obtained. Yield: 45 mg (91%). Anal. Calc for $C_{18}H_{28}CdCl_2N_6O_{12}$ (MW 703.76): C, 30.72; H, 4.01; N, 11.94. Found: C, 31.02; H, 3.92; N, 11.91. Selected FTIR peaks (KBr, cm^{-1}): 3416 (s), 3186 (w), 1670 (s), 1602 (s), 1440 (s), 1116 (s), 1090 (s), 772 (s), 626 (s). UV–Vis (solid state): λ_{max}, 264 nm. Light yellow crystals of **4** suitable for single crystal X-ray diffraction analysis were obtained from the slow evaporation of its methanolic solution after 4 days.

General Protocol used for Cyanosilylation reaction

All reactions were carried out in screw cap glass vials with magnetic stirring. A fine powder sample of **4** activated in a vacuum oven at 90 °C for 10 h was used as the catalyst, unless otherwise noted. In a typical reaction, a mixture of an aldehyde (0.5 mmol) and TMSCN (1 mmol) with a specified amount of catalyst was placed in a capped glass vial to stir at room temperature (25-27 °C) for the indicated time. For example, 0.5 mmol benzaldehyde (53 mg), 1 mmol trimethylsilyl cyanide (TMSCN) (99.2 mg) and 2 mol% of **4** (6.2 mg) were used for initial screening experiments with or without a solvent. Upon removal of the catalyst by centrifugation and filtration from the reaction mixture, the conversion of product in each run was determined by ^1H NMR spectroscopy. For recycling experiments, the used catalyst (separated by centrifugation and filtration) was washed with CH_2Cl_2 and dried in a vacuum oven for the next run as described above.

Single crystal X-ray data collection and refinement

For initial crystal evaluation and data collection, a Kappa APEX II diffractometer (Mo Kα radiation, λ = 0.71073 Å) equipped with a CCD detector was used using the program APEX2.[57] In each case, integration and scaling of the data were performed using the program SAINT[57] to obtain values of F^2 and $\sigma(F^2)$. Data were also corrected for Lorentz and polarization effects. Further processing of data with subroutine XPREP[57] to determine space group and application of an absorption correction (SADABS)[57] generated files necessary for solution and refinement. Using Olex2,[58] the structure was solved with the ShelXT[59] structure solution program using Intrinsic Phasing and refined with the ShelXL[60] refinement package using least squares minimisation. All non-hydrogen atoms were refined with anisotropic displacement parameters. Hydrogen bonding parameters were generated using PLATON.[61,62] Crystallographic parameters and basic information pertaining to data collection and structure refinement for all compounds are summarized in Table 1. The final positional and thermal parameters for all compounds are listed in the CIF files.

Results and discussion

Synthesis

The new ligand **2-BPEG** was synthesized in two steps, where ethylenediamine was first reacted with 2-pyridinecarboxaldehyde in a 1:2 molar ratio at room temperature in methanol under an inert atmosphere for 4 h. The condensed product was reduced with sodium borohydride to get the intermediate 2-BPED. In second step, 2-BPED and 2-bromoacetamide (1: 2 molar ratio) were refluxed in acetonitrile using K_2CO_3 as a base to produce a light yellow solid product with an overall yield of 74% (with no detectable impurity based on NMR data, a sharp melting point and DTA curve). FTIR, ^1H and ^{13}C NMR and MS (ESI-TOF) spectra of **2-BPEG** are shown in Fig. S1-S6, ESI†. Compounds **1**-**4** were prepared and isolated from the one-pot self-assembly reaction of the respective metal salt and **2-BPEG** in methanol under ambient conditions in good yields. The room temperature synthesis of compounds **1**-**4** can be easily scaled-up, uses a green solvent, and has atom economy. Compounds **1**-**4** are insoluble in CH_3CN, C_2H_5OH, CH_2Cl_2, $CHCl_3$, Hexane, EtOAc and ethers but soluble in H_2O, CH_3OH, dimethylformamide and dimethyl sulfoxide. In addition to satisfactory elemental microanalysis, its formula and phase purity were established by FTIR spectroscopy, powder XRD and single crystal X-ray structural analysis.

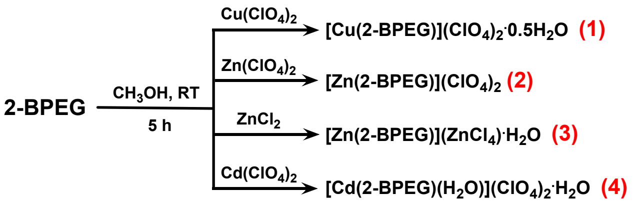

Scheme 1 Synthesis of **1**-**4**.

Spectroscopic characterization

In the FTIR spectra of **1**-**4** (Fig. S7 and S8, ESI†), the presence of an intense peak at around 1665 cm^{-1} is due to the stretching vibration of the coordinated primary amide groups. These peaks are observed at higher wavenumbers compared to the free ligand (1656 cm^{-1}) for the coordination of the primary amide oxygen atoms. Another evidence for the coordination of the ligand through the pyridyl nitrogen atoms is the presence of bands at around 624 cm^{-1}, which could be assigned to the metal-nitrogen stretching vibration. For the presence of lattice perchlorate ion in **1**, **2** and **4**, a very strong peak, which is split and expanded from about 1110 to near 1010 cm^{-1}, is observed; this peak is not observed for **3** due to the absence of perchlorate ions. In all compounds, a peak around 1602 cm^{-1} can be assigned to the C=N stretch of coordinated pyridyl group, which is observed at higher wavenumbers as compared

View Article Online
DOI: 10.1039/C8DT04773A

Table 1 Crystal structure data and refinement parameters for **2-BPEG** and **1-4**

Compound	**2-BPEG**	**1**	**2**	**3**	**4**
Chemical formula	$C_{18}H_{24}N_6O_2$	$C_{18}H_{25}Cl_2CuN_6O_{10.5}$	$C_{18}H_{24}Cl_2N_6O_{10}Zn$	$C_{18}H_{28}Cl_4N_6O_3Zn_2$	$C_{18}H_{28}CdCl_2N_6O_{12}$
Formula Weight (g mol^{-1})	356.43	627.88	620.70	646.99	703.76
Temperature (K)	100 (2)	100 (2)	100 (2)	100 (2)	100 (2)
Wavelength (Å)	0.71073	0.71073	0.71073	0.71073	0.71073
Crystal system	Triclinic	Triclinic	Monoclinic	Monoclinic	Hexagonal
Space group	$P\bar{1}$ (No. 2)	$P\bar{1}$ (No. 2)	$P2_1/c$ (No. 14)	$P2_1/c$ (No. 14)	$P6_522$ (No. 179)
a (Å)	5.9355(10)	10.449(9)	11.448(8)	10.0987(17)	8.9752(2)
b (Å)	8.4642(15)	10.657(10)	15.944(11)	14.915(3)	8.9752(2)
c (Å)	9.5070(17)	12.324(11)	14.769(11)	17.065(4)	57.3894(12)
α (°)	85.012(4)	104.90(2)	90	90	90
β (°)	72.794(3)	100.698(19)	111.007(9)	103.468(13)	90
γ (°)	85.129(3)	93.163(19)	90	90	120
Z	1	2	4	4	6
Volume (Å^3)	453.64(14)	1295(2)	2517(3)	2499.7(9)	4003.6(2)
Density (g/cm^3)	1.305	1.610	1.638	1.719	1.751
μ (mm^{-1})	0.089	1.114	1.253	2.379	1.089
Theta range (°)	2.25 to 25.06	2.00 to 25.00	2.89 to 25.00	2.07 to 25.00	2.13 to 25.03
F(000)	190.0	644.0	1272.0	1312.0	2136.0
Reflections Collected	6468	20718	12104	16625	20558
Independent reflections	1607	4554	4413	4393	2368
Reflections with I >2σ(I)	1263	4094	2525	3044	2309
R_{int}	0.0358	0.0404	0.0836	0.1141	0.0308
Number of parameters	118	349	322	301	186
GOF on F^2	1.023	1.030	1.011	0.936	1.116
Final $R_1{}^a$ / w$R_2{}^b$ ($I > 2\sigma(I)$)	0.0548/0.1561	0.0382/0.1028	0.0624/0.1435	0.0517/0.1082	0.0261/0.0571
$R_1{}^a$/w$R_2{}^b$ (all data)	0.0678/0.1693	0.0428/0.1072	0.1239/0.1787	0.0824/0.1223	0.0272/0.0575
Largest diff. peak and hole (eÅ^{-3})	0.49 and -0.23	0.72 and -0.47	0.77 and -0.70	0.61 and -0.70	0.45 and -0.29
Flack parameter	---	---	---	---	0.003(11)

$^aR_1 = \sum||F_o| - |F_c||/\sum|F_o|$. $^b\mathrm{w}R_2 = [\sum \mathrm{w}(F_o{}^2 - F_c{}^2)^2/\sum \mathrm{w}(F_o{}^2)^2]^{1/2}$, where $\mathrm{w} = 1/[\sigma^2(F_o{}^2) + (aP)^2 + bP]$, $P = (F_o{}^2 + 2F_c{}^2)/3$.

to the free ligand (1592 cm^{-1}). There are several peaks observed in the range of 3100-3550 cm^{-1} for all complexes correspond to ν(–NH$_2$) stretching vibrations. The broad nature of these peaks can be attributed to the presence of hydrogen bonding interactions. On the other hand, the bending frequency for the –CH$_2$ groups is found at ~1450 cm^{-1}. The weak bands appearing in the 1260–1040 cm^{-1} region are characteristic of (C–O) and (C–N) stretching vibrations. The peaks observed in the low frequency region (430–580 cm^{-1}) are due to M–N and M–O stretching vibrations.

To study the electronic transitions, UV-VIS spectra of **2-BPEG** and compounds **1**-**4** (Fig. S9, ESI†) were recorded. For **2-BPEG**, there are two intense bands in the UV region (214 nm and 264 nm), which correspond to the π→π* transitions in the pyridine rings. For **1**-**4**, both bands are observed at similar wavelengths, providing an evidence of π–π interaction observed in their crystal structures (*vide infra*). The blue coloured **1** shows a broad low intensity band at 646 nm, which can be assigned to a *d*–*d* transition in Cu(II).

Phase purity and thermal properties

Powder X-ray diffraction patterns were recorded for **1**-**4** at room temperature (Fig. 2). The respective experimental and simulated (from the single crystal data) patterns of **1**-**4** are similar to each other, confirming that the single crystal and bulk material are the same. It also confirms the phase purity of each bulk sample.

View Article Online
DOI: 10.1039/C8DT04773A

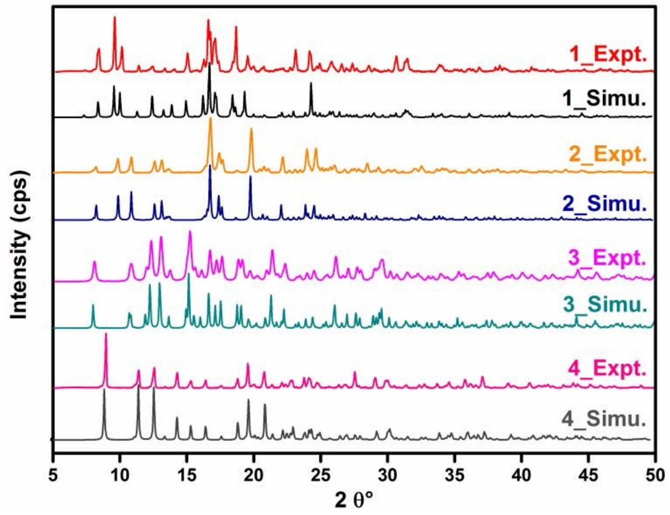

Fig. 2 Experimental and simulated powder X-ray diffraction (PXRD) patterns of **1**-**4**.

Thermogravimetric analyses (TGA) were performed for **2-BPEG** and **4**. The TGA profile shown in Fig. S10 (ESI†) indicates that **2-BPEG** remains thermally stable until 225 °C followed by its degradation. In order to understand the melting point as a function of temperature, differential thermal analysis (DTA) was also carried out. It shows only one major endotherm at 168 °C, which corresponds to its melting temperature, with a melting enthalpy of 285.7 J g^{-1}, whereas other phase transitions were not observed. For **4**, a two-step weight loss profile is observed (Fig. S11, ESI†). In the first step (30−100 °C range), a loss of 5.09% (ca. 5.12%) corresponds to the loss of lattice and coordinated H_2O molecules. Between 100−260 °C, it is stable, after which its decomposition occurs. In order to prove that **4** is stable without the coordinated water molecule (i.e., six-coordinated) between 100−260 °C, the TGA profile of activated **4**, prepared by heating it at 90 °C under vacuum for 10 h, was also carried out. There was no weight loss for the activated **4** between 30−260 °C. This thermal behaviour of **4** is very relevant to its use in catalysis (*vide infra*).

Description of structures

The hydrogen bond parameters for **2-BPEG** and **1-4** are listed in Table 2. The selected bond distances and angles for **2-BPEG** and **1-4** are listed in Table S1 and S2, ESI†, respectively.

2-BPEG

It crystallizes in the triclinic space group $P\bar{1}$ (No. 2) with Z = 1. A labelled ORTEP diagram and unit cell packing diagram of 2-BPEG are shown in Fig. S12 and S13, ESI†, respectively. Through an N–H⋯O hydrogen bonding synthon (d/Å: 2.04, θ/°: 170) between the neighboring molecules, an amide-amide homosynthon with a $R_2^2(8)$ motif is formed, resulting into a ladder-shaped chain structure for 2-BPEG (Fig. 3a). These 1D chains are further extended to a 2D supramolecular network via the other N–H bond and the pyridyl nitrogen of an adjacent molecule with an N–H⋯N hydrogen bonding synthon (d/Å: 2.47, θ/°: 130) (Fig. 3b). Along with this, the 1D chains are also connected *via* the C–H bond of pyridyl group and the amide oxygen of an adjacent molecule with a C–H⋯O hydrogen bonding synthon (d/Å: 2.47, θ/°: 130) (Fig. 3c). It leads to an overall 3D supramolecular network (Fig. 3d).

[Cu(2-BPEG)]$(ClO_4)_2$·0.5H_2O (1)

Like **2-BPEG**, it also crystallizes in the triclinic space group $P\bar{1}$ (No. 2) with Z = 2. The asymmetric unit consists of one 2-BPEG, one Cu(II) ion, two perchlorate anions and one-half lattice water molecule (Fig. S14, ESI†). The Cu(II) centre adopts a six-coordinated distorted octahedral geometry with an N4O2 environment forming five 5-membered chelate rings. The two alkyl nitrogen atoms [N(2) and N(3)] as well as the pyridyl nitrogen atoms [N(1) and N(4)] of the 2-BPEG coordinate with the Cu(II) ion in a *cis* orientation, whereas primary amide oxygen atoms [O(1) and O(2)] coordinate with the Cu(II) ion in a trans orientation. A labelled ORTEP diagram showing the coordination environment around the Cu(II) centre is shown in Fig. 4a. The unit cell packing diagram of **1** is shown in Fig. S15, ESI†. The Cu-N and Cu-O bond lengths fall in the range of 2.019(3)–2.069(3) Å and 2.269(3)–2.358(3) Å, respectively, which are similar to those reported for hexacoordinated Cu(II) with N, O-mixed ligands.[26,62] The elongation of axial bonds [Cu(1)–O(1), 2.269(3) Å and Cu(1)–O(2), 2.358(3) Å] indicates a Z-out Jahn–Teller distortion, as expected for Cu(II) octahedral complexes.[63,64] The basal bond angles are all close to 90°: [O(1)–Cu(1)–N(1), 91.43(9)°; O(1)–Cu(1)–N(2), 93.59(11)°; O(1)–Cu(1)–N(4), 93.11(11)°; O(2)–Cu(1)–N(4), 92.05(11)°; O(2)–Cu(1)–N(3), 90.36(9)°; O(2)–Cu(1)–N(1), 96.61 (10)°; O(2)–Cu(1)–N(3), 90.36 (9)°].

Molecules of **1** are tightly held together by N–H⋯O and C–H⋯O hydrogen bonding (Fig. 4b) and π–π stacking (Fig. 4c) to generate a compact 3D supramolecular network (Fig. 4d). Among the lattice perchlorates and water molecules, only the perchlorates are found to be participating in the hydrogen bonding. Four hydrogen atoms of two NH_2 moieties are involved in hydrogen bonding with perchlorates, where one hydrogen is involved in the bifurcated interaction with two oxygens of a perchlorate ion, forming a $R_2^1(4)$ motif. Along with the N–H⋯O synthon, perchlorates are also contributing to hydrogen bonding with aromatic as well as aliphatic C–H bonds through the C–H⋯O synthon. The C–H bonds of a pyridyl group and the amide oxygen of an adjacent molecule generate two C-H⋯O synthons: i) C(6)–H⋯O(2) (d/Å: 2.48, θ/°: 154) with a dimeric $R_2^2(10)$ motif and (ii) C(10)–H⋯O(1) (d/Å: 2.47, θ/°: 147) with a dimeric $R_2^2(14)$ motif. For the π–π interactions between two aromatic rings of each ligand, the distances are 4.024 Å and 3.827 Å.

[Zn(2-BPEG)]$(ClO_4)_2$ (2)

It crystallizes in the monoclinic space group $P2_1/c$ (No. 14) with Z = 4 with an asymmetric unit consisting of one 2-BPEG, one Zn(II) ions and two lattice perchlorate ions (Fig. S16, ESI†). Like the Cu(II) center in **1**, the Zn(II) centre in **2** is six-coordinated with a distorted octahedron geometry and is surrounded by four nitrogen atoms (two aliphatic and two pyridyl) in equatorial positions and two oxygen atoms (primary amide) in

View Article Online
DOI: 10.1039/C8DT04773A

Table 2 Hydrogen bond parameters with symmetry codes for **2-BPEG** and **1-4**[a]

2-BPEG					
D–H...A	**r (D-H) (Å)**	**r (H…A) (Å)**	**r (D…A) (Å)**	**∠D-H…A (°)**	**Symmetry**
N(3)–H(3A)...O(1)	0.86	2.04	2.896(2)	170	-x,1-y,1-z
N(3 –H(3B)...N(1)	0.86	2.41	2.783(2)	106	---
N(3)–H(3B)...N(2)	0.86	2.47	3.094(2)	130	-1+x,y,z
C(3)–H(3)...O(1)	0.93	2.49	3.360(3)	155	x,-1+y,z
1					
D–H...A	**r (D-H) (Å)**	**r (H…A) (Å)**	**r (D…A) (Å)**	**∠D-H…A (°)**	**Symmetry**
N(5)–H(5A)...O(8)	0.86	2.49	3.052(5)	124	1-x,1-y,-z
N(5)–H(5A)...O(10)	0.86	2.32	3.130(6)	158	1-x,1-y,-z
N(5)–H(5B)...O(4)	0.86	2.21	3.040(6)	161	-x,1-y,-z
N(6)–H(6A)...O(9)	0.86	2.5	3.067(6)	124	-x,-y,-z
N(6)–H(6A)...O(11)	0.86	2.46	3.318(7)	174	-x,-y,-z
N(6)–H(6B)...O(3)	0.86	2.2	3.032(5)	163	-x,-y,-z
C(2)–H(2A)...O(1)	0.97	2.58	3.113(5)	114	---
C(2)–H(2B)...O(9)	0.97	2.42	3.387(6)	178	-x,1-y,-z
C(6)–H(6)...O(2)	0.93	2.48	3.337(5)	154	1-x,1-y,1-z
C(8)–H(8B)...O(3)	0.97	2.54	3.497(6)	168	---
C(10)–H(10)...O(1)	0.93	2.47	3.290(6)	147	-x,1-y,1-z
C(15)–H(15A)...O(8)	0.97	2.54	3.437(6)	153	---
C(16)–H(16)...O(5)	0.93	2.58	3.268(6)	132	1+x,y,z
2					
D–H...A	**r (D-H) (Å)**	**r (H…A) (Å)**	**r (D…A) (Å)**	**∠D-H…A (°)**	**Symmetry**
N(5)–H(5A)...O(3)	0.86	2.34	3.156(8)	159	x,y,-1+z
N(5)–H(5B)...O(8)	0.86	2.20	3.018(9)	157	---
N(6)–H(6B)...O(5)	0.86	2.26	2.983(9)	141	---
C(3)–H(3)...O(1)	0.93	2.52	3.357(8)	149	-x,1-y,-z
C(9)–H(9)...O(3)	0.93	2.50	3.300(8)	145	x,3/2-y,-1/2+z
C(9)–H(9)...O(5)	0.93	2.57	3.251(10)	130	x,3/2-y,-1/2+z
C(15)–H(15A)...O(5)	0.97	2.49	3.435(11)	165	1-x,1-y,1-z
3					
D–H...A	**r (D-H) (Å)**	**r (H…A) (Å)**	**r (D…A) (Å)**	**∠D-H…A (°)**	**Symmetry**
O(3)–H(3A)...Cl(3)	0.85	2.51	3.272(4)	150	2-x,1-y,1-z
O(3)–H(3B)...Cl(1)	0.85	2.37	3.209(4)	168	---
N(5)–H(5A)...Cl(3)	0.88	2.60	3.346(5)	143	2-x,1-y,1-z
N(5)–H(5B)...O(3)	0.88	2.26	2.897(6)	129	---
N(6)–H(6C)...Cl(4)	0.88	2.51	3.364(5)	163	-1+x,y,-1+z
N(6)–H(6D)...Cl(2)	0.88	2.51	3.351(5)	162	1-x,1/2+y,1/2-z
C(3)–H(3)...Cl(4)	0.95	2.74	3.676(5)	169	x,y,-1+z
C(10)–H(10)...Cl(3)	0.95	2.74	3.665(5)	165	1-x,1-y,1-z
C(11)–H(11)...O(1)	0.95	2.44	3.286(7)	148	-x,1-y,-z
C(13)–H(13)...O(2)	0.95	2.49	3.331(7)	148	-x,1-y,-z
C(14)–H(14B)...Cl(1)	0.99	2.82	3.798(6)	169	1-x,1/2+y,1/2-z
C(15)–H(15A)...Cl(2)	0.99	2.81	3.759(6)	160	1-x,1-y,1-z
C(17)–H(17B)...O(3)	0.99	2.43	3.402(7)	166	1-x,1/2+y,1/2-z
4					
D–H...A	**r (D-H) (Å)**	**r (H…A) (Å)**	**r (D…A) (Å)**	**∠D-H…A (°)**	**Symmetry**
O(1)–H(1)...O(4)	0.74	2.43	3.147(5)	165	1-y,1-x,7/6-z
O(1)–H(1)...O(6)	0.74	2.54	3.147(6)	141	1-y,1-x,7/6-z
N(2)–H(2A)...O(7)	0.86	2.09	2.897(6)	156	---
N(2)–H(2B)...O(5)	0.86	2.15	2.961(7)	158	-1+x,y,z
O(7)–H(7)...O(4)	0.80	2.07	2.865(5)	172	---
C(3)–H(3A)...O(5)	0.97	2.42	3.354(8)	160	-y,1-x,7/6-z

[a] Numbers in parenthesis are estimated standard deviations in the last significant digits. D = donor, A = acceptor.

View Article Online
DOI: 10.1039/C8DT04773A

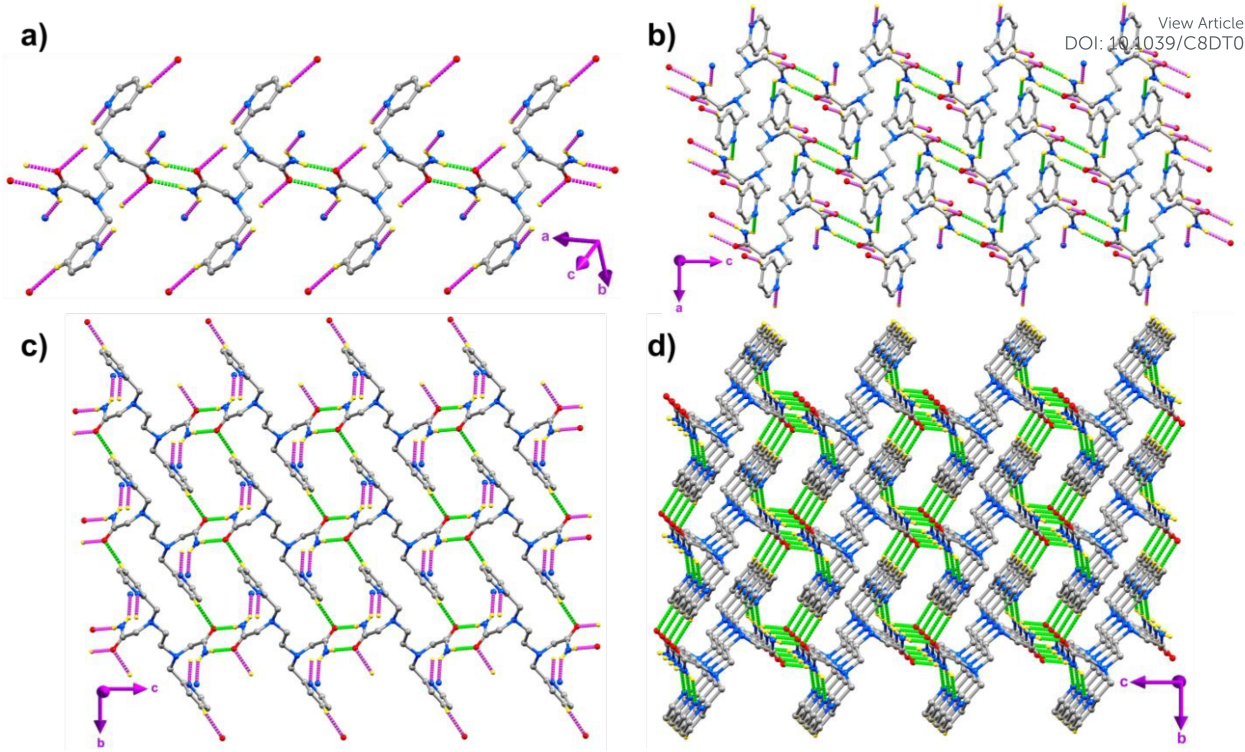

Fig. 3 Schematic representations of **2-BPEG**: (a) a ladder-shaped amide–amide homosynthon *via* strong N–H···O hydrogen bonding interactions; (b, c) 2D supramolecular network along *b* and *a*-axis, respectively; and (d) 3D supramolecular network along *a*-axis. Hydrogens bonded to carbon atoms (without contacts) are hidden to improve clarity. Dotted lines represent hydrogen bonds (violet: hanging contacts and green: expanded contacts).

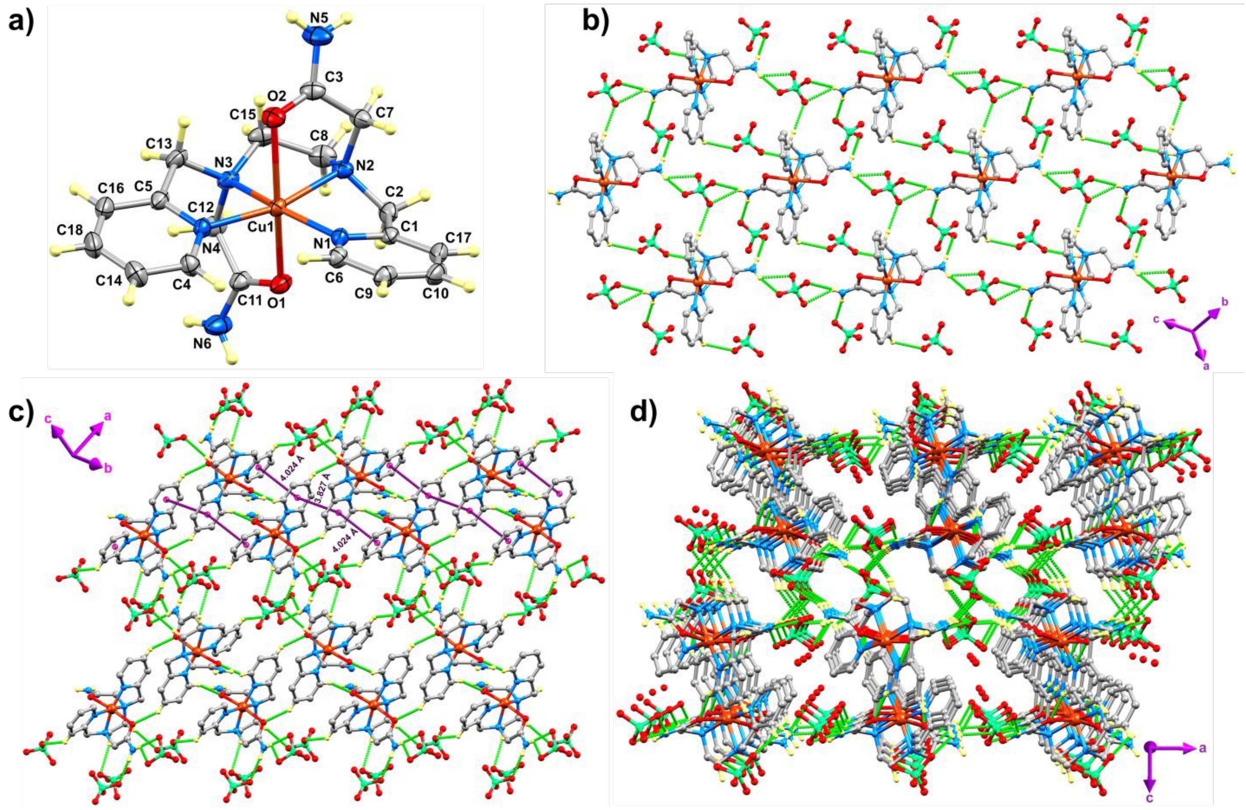

Fig. 4 Schematic representations of **1**: (a) coordination environment around Cu(II) with an atom labelling scheme (non-hydrogen atoms are depicted as ellipsoids with 30% probability); (b) view of 2D supramolecular network formed *via* strong N–H···O and C–H···O hydrogen bonding interactions; (c) view of 2D supramolecular network formed *via* strong π···π interactions (color: violet); and (d) 3D supramolecular network along *b*-axis. Hydrogens bonded to carbon atoms (without contacts) are hidden to improve clarity. Dotted lines (green) represent hydrogen bonds.

View Article Online
DOI: 10.1039/C8DT04773A

axial positions from the 2-BPEG ligand. A labelled ORTEP diagram showing the coordination environment around the Zn(II) centre is shown in Fig. 5a, while its the unit cell packing diagram is shown in Fig. S17, ESI†. The Zn–N and Zn–O distances are in the range of 2.093(5)–2.214(5) Å and 2.156(4)–2.167(4) Å, respectively.

Like **1**, the components of **2** are tightly held together by N–H···O and C–H···O hydrogen bonding and π–π stacking interactions to generate a compact 3D supramolecular network (Fig. 5b). The classical intermolecular N–H···O hydrogen bond between the $-NH_2$ moieties and the perchlorate ions has resulted in a 2D supramolecular network. Unlike **1**, only three hydrogen atoms of two $-NH_2$ moieties of primary amide groups are involved in hydrogen bonding with perchlorate ions, where two distinct perchlorates can be seen; three oxygen atoms of one perchlorate ion and one in the second perchlorate ion participate in hydrogen bonding. Along with the N–H···O synthon, perchlorates are also contributing in hydrogen bonding with aromatic as well as aliphatic C–H groups, through the C–H···O synthon (Fig. S18, ESI†). The C–H bonds of a pyridyl group and the amide oxygen of an adjacent molecule generate two C-H···O synthons: C(6)–H···O(2) (d/Å: 2.52, θ/°: 149) having a dimeric $R_2^2(10)$ motif, and C(10)–H···O(1) (d/Å: 2.47, θ/°: 147) with a dimeric $R_1^2(4)$ motif. These strong C–H···O interactions enable the two aromatic rings of the adjacent ligands to arrange parallel over each other for π–π interactions (3.899 Å) as shown in Fig. S18, ESI†.

[Zn(2-BPEG)](ZnCl$_4$)·H$_2$O (3)

It crystallizes in the monoclinic space group $P2_1/c$ (No. 14) with Z = 4 based on the asymmetric unit consisting of one 2-BPEG, one Zn(II) ions, one lattice water molecule and one lattice tetrachlorozincate(II) ion (Fig. S19, ESI†). Thus, the cation in **3** has the same features found in that of **2** and is not described any further. A labelled ORTEP of the cation in **3** is shown in Fig. 6a, while its unit cell packing diagram is shown in Fig. S20, ESI†. The Zn–N and Zn–O distances are in the range of 2.069(4)–2.207(5) Å and 2.117(4)–2.174(4) Å, respectively.

An overall 3D supramolecular network is generated through the π–π stacking interactions and N–H···Cl, C–H···Cl, O–H···Cl, C–H···O and C–H···Cl hydrogen bonding interactions among the components of **3** (Fig. 6b). All four chlorine atoms of lattice tetrachlorozincate ion are participating in hydrogen bonding, where three chlorine atoms (Cl1, Cl2 and Cl4) are acceptor for two hydrogen atoms each and one chlorine atom (Cl3) is acceptor for three hydrogen atoms which is very rare in the literature. The lattice water molecule also plays a very crucial role, not only its two hydrogen atoms form a O–H···Cl synthon with tetrachlorozincate ion but also it is an acceptor for two hydrogen atoms of one N-H bond and one C-H (aliphatic) bond, forming N–H···O and C–H···O synthons, respectively. The non-classical hydrogen bonding involves four hydrogen atoms of pyridyl group and three aliphatic hydrogen atoms of methylene groups (Fig. S21, ESI†). Further, the C(13)–H···O(2) hydrogen bonding synthon (d/Å: 2.49, θ/°: 148) with a dimeric $R_2^2(10)$ motif involves one C–H bond of a pyridyl group and the amide oxygen of an adjacent molecule. Like **2**, the strong C–H···O interactions in **3** are responsible for intermolecular π–π interactions (3.657 Å) as shown in Fig. S22, ESI†.

[Cd(2-BPEG)(H$_2$O)](ClO$_4$)$_2$·H$_2$O (4)

It crystallizes in the non-centrosymmetric hexagonal space group $P6_522$ (No. 179) with Z = 6. The asymmetric unit consists of half 2-BPEG, one Cd(II) ions with half occupancy, one coordinated water as well as one lattice water molecule with half occupancy and one lattice perchlorate ion (Fig. S23, ESI†).

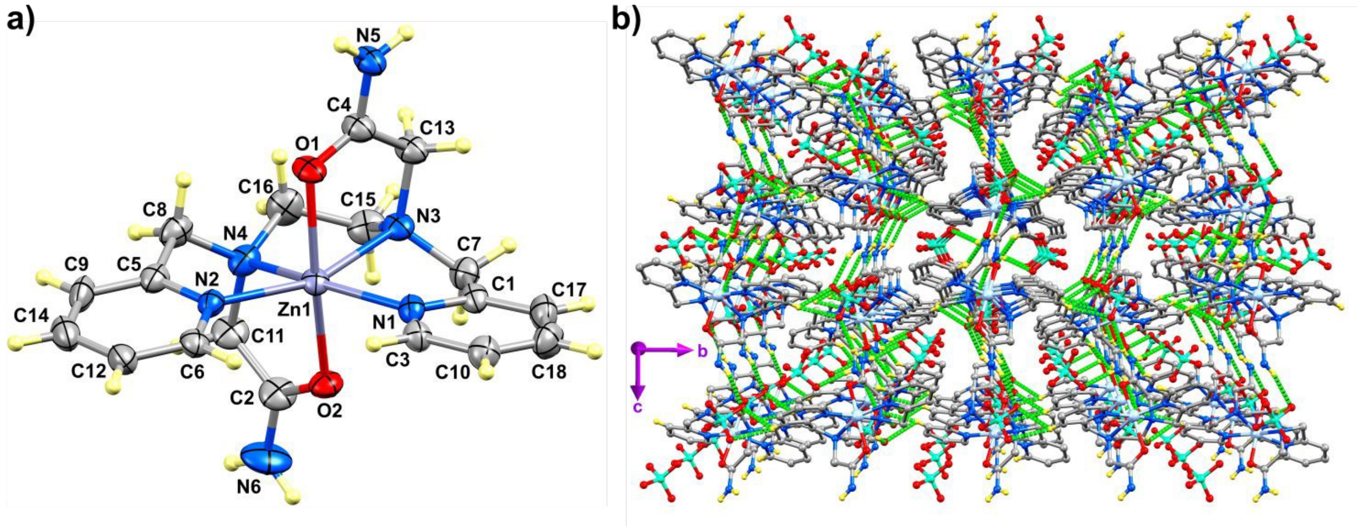

Fig. 5 Schematic representations of **2**: (a) coordination environment around Zn(II) with atom labelling (non-hydrogen atoms are depicted as ellipsoids with 30% probability) and (b) view of 3D supramolecular network along *a*-axis. Hydrogens bonded to carbon atoms (without contacts) are hidden to improve clarity. Dotted lines (green) represent hydrogen bonds.

View Article Online
DOI: 10.1039/C8DT04773A

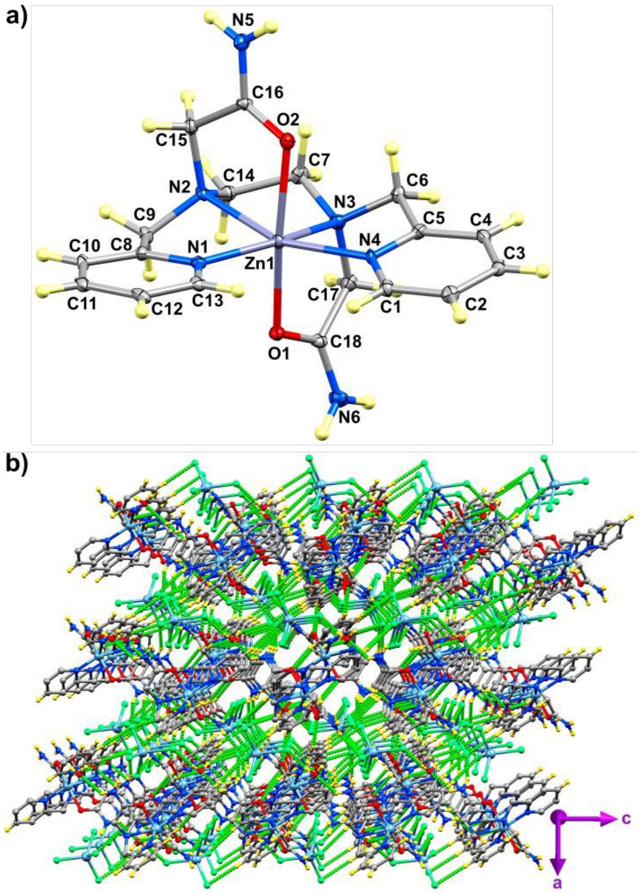

Fig. 6 Schematic representations of **3**: (a) coordination environment around Zn(II) with atom labelling (non-hydrogen atoms are depicted as ellipsoids with 30% probability) and (b) view of 3D supramolecular network along *b*-axis. Hydrogens bonded to carbon atoms (without contacts) are hidden to improve clarity. Dotted lines (green) represent hydrogen bonds.

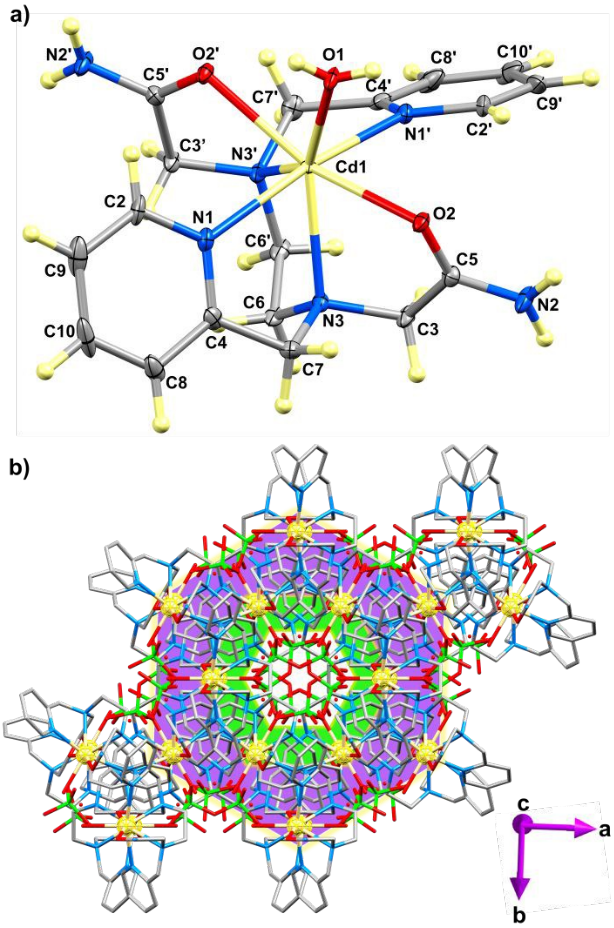

Fig. 7 Schematic representations of **4**: (a) coordination environment around Cd(II) with atom labelling (non-hydrogen atoms are depicted as ellipsoids with 30% probability) and (b) view of hexagonal packing arrangement along *c*-axis. Symmetry operations: ' = x-y, -y, 1-z.

The Cd(II) centre adopts a seven-coordinated distorted pentagonal bipyramidal geometry with an N4O3 environment, where two alkyl nitrogen atoms [N(3) and N(3')], two primary amide oxygen atoms [O(2) and O(2')] and one coordinated water molecule [O(1)] occupy equatorial positions and two pyridyl nitrogen atoms [N(1) and N(1')] occupy axial positions. A labelled ORTEP diagram of the cation in **4** is shown in Fig. 7a. Its unit cell packing is shown in Fig. S24, ESI†. The Cd–N and Cd–O distances are in the range of 2.412(4)–2.414(3) Å and 2.278(4)–2.367(3) Å, respectively.

The components of **4** are tightly held together *via* classical and non-classical hydrogen bonding interactions, such as N–H···O, O–H···O and C–H···O to generate a compactly packed 3D structure (Fig. 7b and S25, ESI†). The perchlorate ion and lattice water molecule play a crucial role in generating supramolecular network with –NH_2, aliphatic C–H and coordinated water molecule. The hydrogen atoms of coordinated water molecules show bifurcated hydrogen bonding with two oxygen atoms of the perchlorate ion resulting in a $R_1^2(4)$ ring. Out of four oxygen atoms of a perchlorate, three are involved in hydrogen bonding with N(2)–H(2B)···O(5), O(7)–H···O(4), O(1)–H(1)···O(6) and O(1)–H(1)···O(5). Through classical intermolecular hydrogen bonding interactions, four different types of motif like $R_1^2(4)$, $R_4^4(14)$, $R_3^2(10)$ and $R_4^6(17)$ are formed as shown in Fig S26, ESI†. Unlike **1**-**3**, the primary amide oxygen atoms in **4** are not participating in any kind of hydrogen bonding interactions.

An overlay of the molecular structures of cations in **1**-**3** (Fig. 8) indicates that (a) a change in metal center from Cu(II) to Zn(II) in **1** and **2** causes prominent changes in conformational flexibility as well as in bond length and angles, and (b) a very little conformational change is there between **2** and **3** due to a variation in the anions.

View Article Online
DOI: 10.1039/C8DT04773A

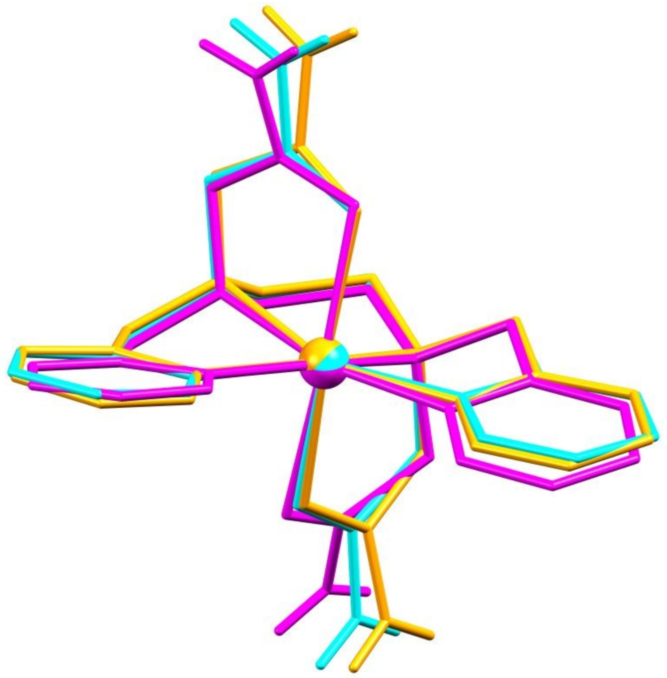

Fig. 8 Overlay of the molecular structures of cations in **1**-**3** (shown in pink, cyan and orange color, respectively). Hydrogen atoms bonded to carbon atoms are hidden to improve clarity.

Study of intermolecular interactions by Hirshfeld surface analysis

For the quantification of intermolecular interactions present in the solid state structures of **1-4**, both Hirshfeld surface analysis[36,63] (HSs) and 2D fingerprint plots[35] (FPs) are utilized. This is an attempt to visualize the proportion and nature of the interactions present in the structures more than those obtained through an examination of their crystal structure alone. To generate the HSs and FPs using Crystal Explorer 3.1[64] based on results of single crystal X-ray diffraction studies, bond lengths to hydrogen atoms were set to standard values. In this regard, a function d_{norm}, which is a ratio encompassing the distances of any surface point to the nearest interior (d_i) and exterior (d_e) atom and the van der Waals radii of the atoms, is defined below.[65]

$$d_{norm} = \frac{\left(d_i - r_i^{vdW}\right)}{r_i^{vdW}} + \frac{\left(d_e - r_e^{vdW}\right)}{r_e^{vdW}}$$

Where, r_i^{vdW} and r_e^{vdW} are the van der Waals radii of the atoms. d_{norm} displays a surface with a red–white–blue colour scheme as follows: the bright red regions with the negative values of d_{norm} represent the intermolecular contacts shorter than the sum of the van der Waals radii; blue regions with positive values of d_{norm} represent the intermolecular contacts longer than the sum of the van der Waals radii; white regions denote the distance of contacts exactly corresponding to the van der Waals separation with a d_{norm} values of zero. Molecular Hirshfeld surfaces in the crystal structure are constructed based on the electron distribution calculated as the sum of spherical atom electron densities. For a given crystal structure and set of spherical atomic electron densities, the Hirshfeld surface is unique. The existence of different types of intermolecular interactions is recognized by a 2D fingerprint plot (d_i versus d_e). Hirshfeld surfaces of **2-BPEG** and **1-4** are illustrated in Fig. S27, ESI†, showing the surfaces that have been mapped over a d_{norm} range of −0.18 to 1.4 Å, a shape index of −1.0 to 1.0 Å and a curvedness of −4.0 to 0.4 Å, respectively.[66] The red regions on the d_{norm} surface represent the significant N–H⋯O, C–H⋯O interactions, and the blue regions and white regions represent the C⋯H and H⋯H interactions, respectively. The shape index is most sensitive to very subtle changes in surface shape; the red/orange triangles on them represent concave regions indicating atoms of the π⋯π stacked molecule above them.[63] The curvedness is the measurement of "how much shape"; the flat areas of the surface correspond to low values of curvedness, while sharp curvature areas correspond to high values of curvedness, indicating interactions between neighbouring molecules.[63] The large flat region indicated by a blue outline on the curvedness surface refers to the π⋯π stacking interactions of the molecule. The red-yellow colored patches present on the flat surface indicate that there is a stacking interaction between the molecules. The π⋯π stacking information conveyed by the shape index and curvedness plots are consistent with the crystal structure analyses.

Quantitative crystal structure analysis

The Hirshfeld surface fingerprint plot is a unique tool as it provides quantitative information about the individual contribution of the intermolecular interaction in the crystal packing. These were generated using a pair of distances (d_e, d_i) for each individual surface spot which is defined as d_i, the distance from the surface to the nearest atom in the molecule itself and d_e, the distance from the surface to the nearest atom in another molecule. Some distinct spikes appearing in the 2D fingerprint plot indicate the different interactions motifs in the crystal lattice. The complementary regions are visible in the fingerprint plots where one molecule acting as a donor ($d_e > d_i$) and the other acting as an acceptor ($d_e < d_i$) can be also identified in the fingerprint plots (FPs).

The intermolecular interactions involved in the **2-BPEG** and **1-4** present as distinct spikes in the fingerprint plot and the proportions of individual interactions are introduced in Fig. S28-S32, ESI†. The graphical representation of the percentage distribution of different interactions present in **2-BPEG** and **1-4** as obtained from the fingerprint plots are shown in Fig. 9.

In case of **2-BPEG**, the maximum contribution in the fingerprint plot is from H⋯H contacts (54.3%). This high contribution can be attributed to the presence of NH_2 of the primary amide group, which involves the existence of dispersion interactions as discussed earlier. Two sharp spikes pointing towards the lower left of the plot are typical H⋯O (17.8%) and H⋯N (11.2%) contacts. For the N⋯H contacts contribution is from pyridyl nitrogen and amide containing N–H forming the N–H⋯N synthon. The next contribution is from C⋯H contacts (14.8%) on account of the presence of C–H⋯π interactions. The remaining area of the fingerprint plot is

View Article Online
DOI: 10.1039/C8DT04773A

occupied by a minor (<1.1%) contribution from C···C, O···C, and O···O interactions. Similarly, Hirshfeld surface analyses of **1**-**4** show a similar type of contributions of H···H interactions (> 30%) due to the presence of NH_2 of the primary amide group. In **1**, **2** and **4**, the highest contribution is from H···O interactions, 50.8, 46.2 and 43.9%, respectively. It can be attributed to C–H···O and N–H···O interactions, due to the involvement of primary amide oxygen and perchlorate oxygen atoms in hydrogen bonding. These are in agreement with the X-ray crystallographic analysis of hydrogen bonding interactions. In **3**, a sharp spike pointing towards lower left is from second highest contribution of H···Cl (22.7%) interaction after H···H (43.6%), this can be due to C–H···Cl and N–H···Cl interactions, due to the participation of tetrachlorozincate ions in hydrogen bonding and also the close packing of tetrachlorozincate anion and cation, which can be seen in Fig. S20, ESI†.

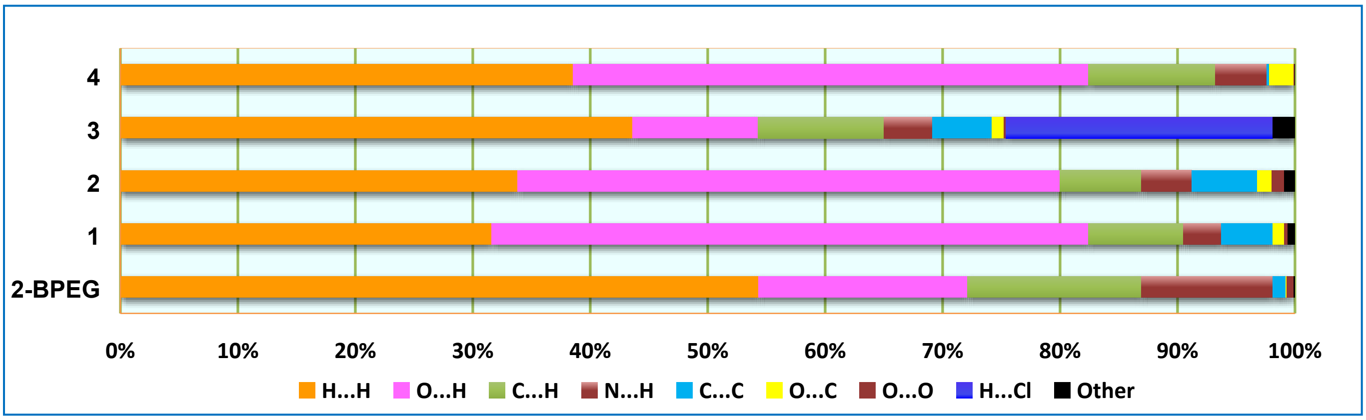

Fig. 9 Graphical representation of the percentage contributions of all type interactions overlapping in the 2D fingerprint plots for **2-BPEG** and **1-4**.

Catalysis studies

Among the four compounds in this study, compound **4** was logically chosen based on the reasons provided earlier for catalysis studies. Considering the fact that activated **4** can have a coordinatively unsaturated metal center due to the presence of a coordinated water molecule in it, its potential as a Lewis acid catalyst for the cyanosilylation reaction of aldehyde was tested. Prior to the use of **4** in catalysis, it was activated under vacuum at 90 °C for 10 h (based on its TGA profile, vide supra). As evident from the TGA, FTIR spectra, and PXRD patterns (Fig. S11, S33 and S34, respectively, ESI†), an unsaturated Cd(II) metal center is generated without losing its structural integrity.

To carry out the reaction under heterogeneous conditions, various solvents such as hexane, dichloromethane, chloroform, acetonitrile and ethanol were chosen since the catalyst is insoluble in these solvents. Initial optimization studies were carried out between benzaldehyde and TMSCN as substrates in these solvents as well as in solvent-free conditions at room temperature (25-27 °C) using 2 mol% of **4** for 10 h (Table 3, entries 1-6). An example of measuring the % conversion by ^{1}H NMR spectroscopy is reported in Fig. S35, ESI†. As the product conversions varied between 22-70% in these solvents, the reaction

Table 3 Optimization of reaction parameters for the Cyanosilylation reaction between benzaldehyde and trimethylsilyl cyanide (TMSCN) at room temperature (25-27 °C)[a]

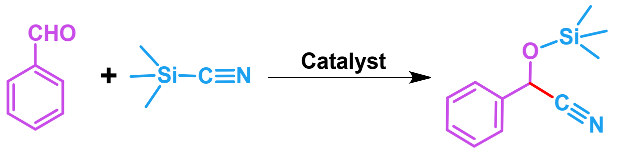

Entry	Catalyst	Time (h)	Catalyst (mol %)	Solvent	Conversion (%)
1	4	10	2	CH_3CN	39
2	4	10	2	C_2H_5OH	22
3	4	10	2	CH_2Cl_2	67
4	4	10	2	$CHCl_3$	65
5	4	10	2	Hexane	70
6	**4**	**10**	**2**	**---**	**>99**
7	4	10	0.5	---	85
8	4	10	1	---	92
9	4	10	3	---	>99
10	4	8	2	---	97
11	4	6	2	---	85
12	4	4	2	---	74
13	4	2	2	---	65
14	4	1	2	---	46
15	2-BPED	10	2	---	13
16	2-BPEG	10	2	---	15
17	$Cd(ClO_4)_2$	10	2	---	22
18[b]	4	10	2	---	22
19	-----	10	2	---	8

[a]Reaction conditions: benzaldehyde (0.5 mmol), TMSCN (1 mmol) and 1 mL solvent. The reaction temperature was kept at 25-27 °C throughout the reaction. Average conversion for a set of triplicate runs, calculated by ^{1}H NMR spectroscopy. [b]Catalyst used as-synthesized (without activation).

View Article Online
DOI: 10.1039/C8DT04774A

rate was found to be solvent dependent in the following order: hexane > dichloromethane > chloroform > acetonitrile > ethanol. This indicates that the highest conversion is obtained in a nonpolar solvent while the lowest conversion is observed in a protic solvent. Furthermore, the conversion in an alcoholic solvent is affected by its consumption of the TMSCN reagent. On the other hand, the highest product conversion (>99%) was acquired under solvent-free condition. Under the solvent-free condition, the catalyst amount was varied from 0.5 mol% to 3 mol% (Table 3, entries 7-9) to confirm that 2 mol% catalyst is the minimum required for >99% conversion. However, the reaction was time-dependent, and a decrease in reaction time led to a significant decrease in the conversion (Table 3, entries 10-14). A plot of conversion versus time for the reaction of benzaldehyde and TMSCN is presented in Fig. 10, showing that 10 h is the best reaction time.

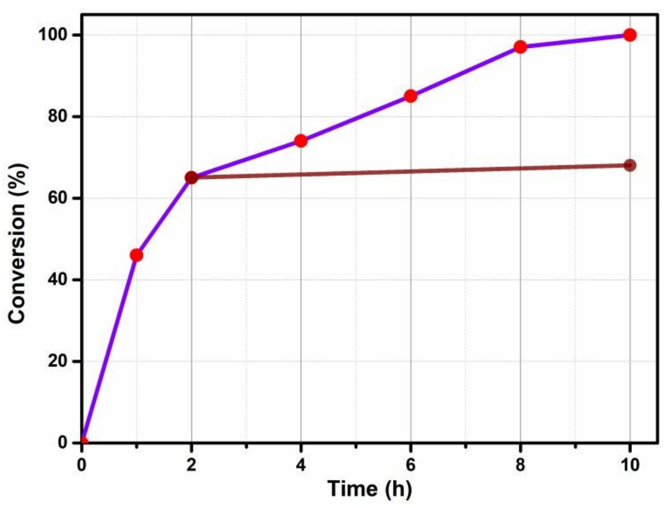

Fig. 10 Plot of conversion *vs* time (violet curve) for **4**; its heterogeneous nature is demonstrated by its removal from the reaction mixture at 2 h followed by further stirring until 10 h (brown line).

For comparison, a series of control experiments were also carried out (Table 3, entries 15-19). Use of the ligands (2-BPED or 2-BPEG) only as a catalyst resulted in conversion of 13% and 15%, respectively, under the same conditions. Additionally, using $Cd(ClO_4)_2.XH_2O$ instead of **4**, a conversion of 22% was obtained. The Cd^{2+} ion in $Cd(ClO_4)_2{\cdot}XH_2O$ is blocked by the coordinated water molecules, making it more difficult to access by the substrates. On the other and, the use of as-synthesized **4** (unactivated) under similar conditions resulted in only 22% conversion (Table 3, entry 18). These observations reveal the catalytic sites are ascribed to the unsaturated metal centers. Obviously, when the reaction was carried out in absence of **4**, only 8% conversion was observed (Table 3, entry 19). This demonstrates the excellent catalytic performance of **4** for the formation of a C–C bond.

In order to get an insight into the effect of different substituents in aromatic aldehydes, a variety of benzaldehyde derivatives were selected as substrates (Table 4). It is found that those bearing electron-withdrawing groups were completely converted to the corresponding cyanosilylation products after 10 h. Whereas, those with electron-donating groups resulted in markedly reduced product formation (63-74%) under the same conditions. The observed difference in the catalytic performance of **4** toward the benzaldehyde derivatives can be attributed to the fact that the electron-withdrawing groups in the benzaldehyde derivatives increases the electropositive charge on the aldehyde group, leading to excellent conversions in the nucleophilic cyanosilylation reaction.

Table 4 Substrate scope of aldehyde in cyanosilylation reaction catalysed by **4**[a]

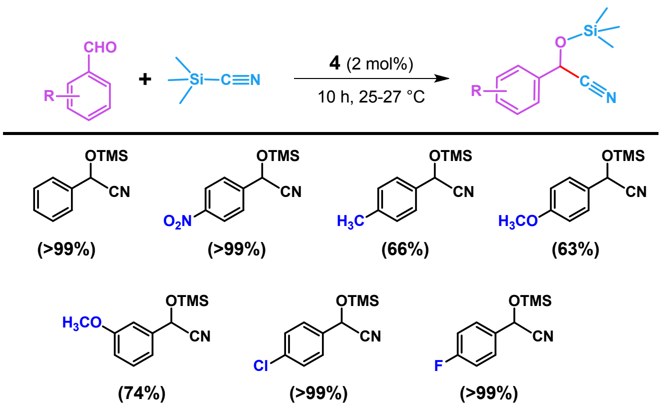

[a]Reaction conditions: aldehyde (0.5 mmol), TMSCN (1 mmol) and **4** (2 mol%) at 25-27 °C. Numbers in parenthesis are average % conversion for a set of triplicate runs, calculated by ^1H NMR spectroscopy.

The recovery of **4** from the reaction is easy by centrifugation and filtration, and it can be reused several times without any significant loss of catalytic activity. After the first cycle, the recovered catalyst was washed thoroughly with CH_2Cl_2 and dried under vacuum. The performance of the recycled catalyst in the cyanosilylation reaction was evaluated using benzaldehyde as the substrate. As illustrated in Fig. 11, the conversion of the benzaldehyde in five successive runs remained almost the same in every run. To check the stability of the recovered catalyst, it was thoroughly characterized by PXRD and FTIR spectroscopy. Comparison of PXRD patterns and FTIR spectra (see Fig. S34 and S36, ESI† respectively) of the pristine and recovered catalyst persuasively demonstrated the retention of structural integrity of **4** after the reaction.

To clarify whether the catalytic process is heterogeneous or homogeneous in nature, the hot filtration experiment was performed. A control experiment was conducted with **4** until an intermediate conversion (ca. 65%) was observed (after 2 h) and then the catalyst was removed by centrifugation and filtration. The catalyst-free reaction mixture was stirred under the same conditions for additional 8 h. As shown in Fig. 10 (brown line), after removal of the solid catalyst, the conversion did not increase significantly. These results demonstrate that the reaction catalysed by **4** is heterogeneous in nature.

In comparison with other reported coordination polymers and complexes as heterogeneous catalysts for cyanosilylation reaction of benzaldehyde and TMSCN, catalyst **4** is among the best ones in terms of catalyst loading, solvent, reaction time, conversion and recyclability (*vide infra*). For example, a hydrothermally synthesized discrete *penta*-coordinated Pb(II)

View Article Online
DOI: 10.1039/C8DT04773A

complex[45] promoted this reaction up to 96% conversion (conditions: 3 mol% catalyst, 16 h and dichloromethane as solvent). Very recently, Cai *et al*. reported[48] a solvothermally synthesized 1D infinite chain of Cd(II) of a secondary amide-based ligand, which gave a >99% conversion in 8 h using 2 mol% catalyst and n-hexane as the solvent. Another hydrothermally synthesized $Cu_3(BTC)_2$, also known as HKUST-1, offered only moderate conversion of 57% after prolonged duration (72 h) with a high catalyst loading of 5 mol% at 50 °C.[49] A lanthanide–organic framework $Tm(BDC)_{1.5}$ afforded a moderate conversion of 57% of benzaldehyde after 5 h.[50] A microporous metal organic framework $Mn_3[(Mn_4Cl)_3(BTT)_8(CH_3OH)_{10}]_2$ provided a 98% conversion with 11 mol % catalyst after 9 h in dichloromethane.[51] Moreover, the Co(II) and Ni(II) based heterometallic coordination polymers resulted in 77% product formation by using 10% of the catalyst at 50 °C for 16 h.[52] In addition to the above mentioned advantages, compound **4** was synthesized under ambient conditions in less time with readily available and cheap starting materials. Therefore, compound **4** appears to be a much more efficient catalyst than other reported ones for this reaction.

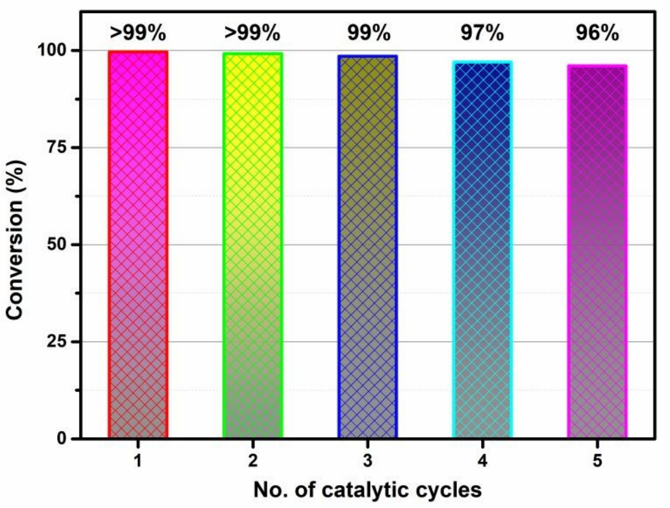

Fig. 11 Plot of % Conversion for five consecutive cycles of the cyanosilylation reaction of benzaldehyde and TMSCN catalysed by **4**.

Conclusions

In summary, we have utilized a new primary amide based flexible, symmetrical and neutral **2-BPEG** ligand to make four novel cationic metal complexes of Cu(II), Zn(II) and Cd(II) at room temperature. Their single crystal X-ray structures have revealed very interesting 3D supramolecular coordination networks. All these complexes exhibit remarkable N–H···O interactions in their solid state structures. The usefulness of the primary amide functionality and tetrahedral ions like ClO_4^- and $ZnCl_4^{2-}$ in the construction of supramolecular networks is clearly explained, making these as very important tools for crystal engineering. These anions having four hydrogen bond acceptor atoms strongly interact with hydrogen bond donor atoms (selected N-H and C-H bonds in the coordinated 2-BPEG ligand of **1**-**4**) present within these compounds in different directions to enhance crystal stability. Furthermore, various *trimeric* to *hexameric* hydrogen bond ring motifs are found in their crystal structures. The amide moiety participates in these motifs usually as a double proton donor, along with the anions (ClO_4^- and $ZnCl_4^{2-}$) and water molecules. Moreover, the role of weak intermolecular interactions in the crystal packing of **2-BPEG** and **1**-**4** has been analysed and quantified using Hirshfeld surface analysis. This work provides an in-depth understanding of structural properties of supramolecular coordination architectures and will contribute to achieving the desired rational design of new materials with more predictable solid-state structures.

Taking advantage of an open Lewis acid site in **4**, it was used as an efficient heterogeneous catalyst for the solvent-free cyanosilylation of various aldehydes with TMSCN producing the corresponding trimethylsilyl ether (precursor of the cyanohydrins) in high yields with a very little catalyst load. Importantly, **4** shows much higher catalytic activities for the benzaldehyde derivatives with electron-withdrawing as well as electron-donating groups.

In continuation of this research, we plan to introduce other metal centers and different counter anions to explore their effect on the coordination environment and hydrogen bond motifs, e.g., the composition and size of the ring. Future studies will also be directed toward developing cheaper, more stable, or even chiral primary amide-based metal complexes for asymmetric transformations.

Conflicts of interest

There are no conflicts to declare.

Acknowledgements

Funding for this work was provided by IISER, Mohali. D. M. is grateful to the UGC of India for a research fellowship. The use of X-ray and NMR central facilities and other departmental facilities at IISER Mohali and CIL, NIPER, Mohali for CHN analysis, is acknowledged.

Notes and references

1 A. R. Hirst, B. Escuder, J. F. Miravet and D. K. Smith, *Angew. Chemie Int. Ed.*, 2008, **47**, 8002–8018.
2 M.-C. Daniel and D. Astruc, *Chem. Rev.*, 2004, **104**, 293–346.
3 N. H. Evans and P. D. Beer, *Angew. Chemie Int. Ed.*, 2014, **53**, 11716–11754.
4 X. Ma and Y. Zhao, *Chem. Rev.*, 2015, **115**, 7794–7839.
5 C. Janiak, *Dalton Trans.*, 2003, 2781–2804.
6 T. R. Cook, Y. Zheng and P. J. Stang, *Chem. Rev.*, 2013, **113**, 734–777.
7 C. B. Aakeröy, J. Desper and J. Valdés-Martínez, *CrystEngComm*, 2004, **6**, 413–418.
8 A. B. Descalzo, R. Martínez-Máñez, F. Sancenón, K. Hoffmann and K. Rurack, *Angew. Chemie Int. Ed.*, 2006, **45**, 5924–5948.
9 K. Ariga, J. P. Hill, M. V Lee, A. Vinu, R. Charvet and S. Acharya, *Sci. Technol. Adv. Mater.*, 2008, **9**, 014109.

View Article Online
DOI: 10.1039/C8DT04773A

10 M. D. Ward and P. R. Raithby, *Chem. Soc. Rev.*, 2013, **42**, 1619–1636.

11 B. J. Holliday and C. A. Mirkin, *Angew. Chem. Int. Ed. Engl.*, 2001, **40**, 2022–2043.

12 G. R. Desiraju, *J. Chem. Soc. Dalton Trans.*, 2000, 3745–3751.

13 G. R. Desiraju, *Crystal Design: Structure and Function*, John Wiley & Sons, Ltd, Chichester, UK, 2003.

14 J.-M. Lehn, *Supramolecular Chemistry: Concepts and Perspectives*, Wiley-VCH Verlag GmbH & Co. KGaA, Weinheim, FRG, 1995.

15 G. R. Desiraju and T. Steiner, *The Weak Hydrogen Bond*, Oxford University Press, 2001.

16 X. He, Y. Yao, X. Luo, J. Zhang, Y. Liu, L. Zhang and Q. Wu, *Organometallics*, 2003, **22**, 4952–4957.

17 X.-L. Zhao and W.-Y. Sun, *CrystEngComm*, 2014, **16**, 3247–3258.

18 M. Chen, S.-S. Chen, T. Okamura, Z. Su, M.-S. Chen, Y. Zhao, W.-Y. Sun and N. Ueyama, *Cryst. Growth Des.*, 2011, **11**, 1901–1912.

19 J. An, O. K. Farha, J. T. Hupp, E. Pohl, J. I. Yeh and N. L. Rosi, *Nat. Commun.*, 2012, **3**, 604.

20 S. Kitagawa, R. Kitaura and S. Noro, *Angew. Chemie Int. Ed.*, 2004, **43**, 2334–2375.

21 N. Smrečki, B.-M. Kukovec, M. Đaković and Z. Popović, *Polyhedron*, 2015, **93**, 106–117.

22 N. Smrečki, V. Stilinović, O. Jović, B.-M. Kukovec and Z. Popović, *Inorganica Chim. Acta*, 2017, **462**, 57–63.

23 H. Maumela, R. D. Hancock, L. Carlton, J. H. Reibenspies and K. P. Wainwright, *J. Am. Chem. Soc.*, 1995, **117**, 6698–6707.

24 M. K. C. T. Nagata, P. S. Brauchle, S. Wang, S. K. Briggs, Y. S. Hong, D. W. Laorenza, A. G. Lee and T. D. Westmoreland, *Polyhedron*, 2016, **114**, 299–305.

25 N. Smrečki, O. Jović, K. Molčanov, B.-M. Kukovec, I. Kekez, D. Matković-Čalogović and Z. Popović, *Polyhedron*, 2017, **130**, 115–126.

26 N. W. Alcock, G. Clarkson, P. B. Glover, G. A. Lawrance, P. Moore and M. Napitupulu, *Dalton Trans.*, 2005, 518–527.

27 H. Sigel and R. B. Martin, *Chem. Rev.*, 1982, **82**, 385–426.

28 C. B. Aakeröy, *Chem. Commun.*, 1998, 1067–1068.

29 D. Markad and S. K. Mandal, *CrystEngComm*, 2017, **19**, 7112–7124.

30 S. K. Mandal and L. Que, *Inorg. Chem.*, 1997, **36**, 5424–5425.

31 J. C. Mareque Rivas, R. Torres Martín de Rosales and S. Parsons, *Dalton Trans.*, 2003, 2156–2163.

32 K. Sakai, T. Imakubo, M. Ichikawa and Y. Taniguchi, *Dalton Trans.*, 2006, 881–883.

33 C. R. Groom, I. J. Bruno, M. P. Lightfoot and S. C. Ward, *Acta Crystallogr. Sect. B Struct. Sci. Cryst. Eng. Mater.*, 2016, **72**, 171–179.

34 A. K. Gupta, K. Tomar and P. K. Bharadwaj, *CrystEngComm*, 2017, **19**, 2253–2263.

35 J. J. McKinnon, D. Jayatilaka and M. A. Spackman, *Chem. Commun.*, 2007, **267**, 3814–3816.

36 J. J. McKinnon, A. S. Mitchell and M. A. Spackman, *Chem. - A Eur. J.*, 1998, **4**, 2136–2141.

37 T. Hökelek, V. Yavuz, H. Dal and H. Necefoğlu, *Acta Crystallogr. Sect. E Crystallogr. Commun.*, 2018, **74**, 45–50.

38 R. J. H. Gregory, *Chem. Rev.*, 1999, **99**, 3649–3682.

39 J.-M. Brunel and I. P. Holmes, *Angew. Chemie*, 2004, **116**, 2810–2837.

40 M. North, D. L. Usanov and C. Young, *Chem. Rev.*, 2008, **108**, 5146–5226.

41 W. K. Cho, J. K. Lee, S. M. Kang, Y. S. Chi, H. S. Lee and I. S. Choi, *Chem. - A Eur. J.*, 2007, **13**, 6351–6358.

42 D. Kumar, A. P. Prakasham, S. Das, A. Datta and P. Ghosh, *ACS Omega*, 2018, **3**, 1922–1938.

43 N. Kurono and T. Ohkuma, *ACS Catal.*, 2016, **6**, 989–1023.

44 J.-M. Brunel and I. P. Holmes, *Angew. Chemie Int. Ed.*, 2004, **43**, 2752–2778.

45 A. Karmakar, S. Hazra, M. F. C. Guedes Da Silva and A. J. L. Pombeiro, *Dalton Trans.*, 2015, **44**, 268–280.

46 M. Lakshmi Kantam, K. Mahendar, B. Sreedhar, K. Vijay Kumar and B. M. Choudary, *Synth. Commun.*, 2008, **38**, 3919–3936.

47 H. An, Y. Zhang, Y. Hou, T. Hu, W. Yang, S. Chang and J. Zhang, *Dalton Trans.*, 2018, **47**, 9079–9089.

48 L. Hu, G. X. Hao, H. D. Luo, C. X. Ke, G. Shi, J. Lin, X. M. Lin, U. Y. Qazi and Y. P. Cai, *Cryst. Growth Des.*, 2018, **18**, 2883–2889.

49 K. Schlichte, T. Kratzke and S. Kaskel, *Microporous Mesoporous Mater.*, 2004, **73**, 81–88.

50 H. He, H. Ma, D. Sun, L. Zhang, R. Wang and D. Sun, *Cryst. Growth Des.*, 2013, **13**, 3154–3161.

51 S. Horike, M. Dincă, K. Tamaki and J. R. Long, *J. Am. Chem. Soc.*, 2008, **130**, 5854–5855.

52 J. J. Du, X. Zhang, X. P. Zhou and D. Li, *Inorg. Chem. Front.*, 2018, **5**, 2772–2776.

53 M. Fujita, Y. J. Kwon, S. Washizu and K. Ogura, *J. Am. Chem. Soc.*, 1994, **116**, 1151–1152.

54 H. Hattori, *Chem. Rev.*, 1995, **95**, 537–558.

55 O. Ohmori and M. Fujita, *Chem. Commun.*, 2004, **4**, 1586–1587.

56 M. Tretbar and C. B. W. Stark, *Eur. J. Org. Chem.*, 2017, **46**, 6942–6946.

57 *APEX2, SADABS and SAINT*, Bruker AXS Inc, Madison, WI, USA, 2008.

58 O. V. Dolomanov, L. J. Bourhis, R. J. Gildea, J. A. K. Howard and H. Puschmann, *J. Appl. Crystallogr.*, 2009, **42**, 339–341.

59 G. M. Sheldrick, *Acta Crystallogr. Sect. A Found. Adv.*, 2015, **71**, 3–8.

60 G. M. Sheldrick, *Acta Crystallogr. Sect. C Struct. Chem.*, 2015, **71**, 3–8.

61 A. L. Spek, *PLATON, Version 1.62*, University of Utrecht, 1999.

62 A. L. Spek, *J. Appl. Crystallogr.*, 2003, **36**, 7–13.

63 M. A. Spackman and D. Jayatilaka, *CrystEngComm*, 2009, **11**, 19–32.

64 S. K. Wolff, D. J. Grimwood, J. J. McKinnon, M. J. Turner, D. Jayatilaka and M. A. Spackman, *CrystalExplorer 3.1*, University of Western Australia, 2012.

65 F. L. Hirshfeld, *Theor. Chim. Acta*, 1977, **44**, 129–138.

66 J. J. Koenderink and A. J. van Doorn, *Image Vis. Comput.*, 1992, **10**, 557–564.

View Article Online
DOI: 10.1039/C8DT04773A

Table of Contents Artwork

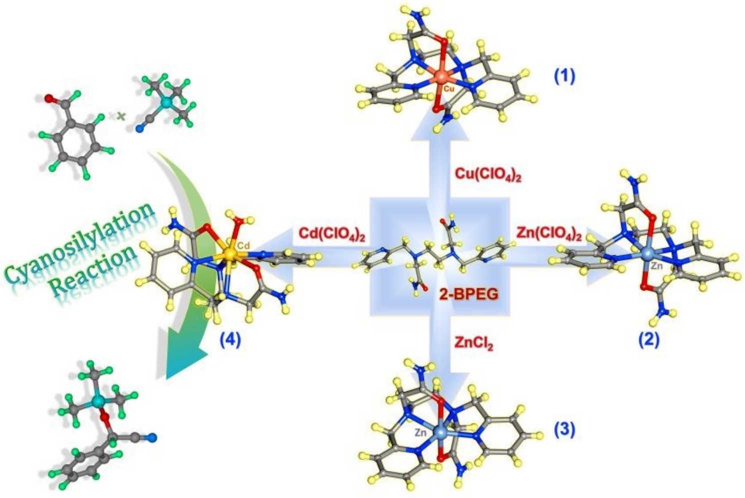

Using a new primary amide functionalized ligand **2-BPEG**, four novel metal complexes of Cu(II), Zn(II) and Cd(II) have been synthesized and fully characterized. For the solvent-free cyanosilylation reaction of an aldehyde with TMSCN, the Cd(II) analogue is found to be an excellent heterogeneous catalyst.